Sensors & Actuators: B. Chemical 424 (2025) 136866

Contents lists available at ScienceDirect

Sensors and Actuators: B. Chemical

journal homepage: www.elsevier.com/locate/snb

Rapid detection of microbial antibiotic susceptibility via deep learning supported analysis of angle-resolved scattered-light images of picoliter droplet cultivations

Martina Graf [a,b,1], Arjun Sarkar [b,c,1], Carl-Magnus Svensson [c], Anne-Sophie Munser [d], Sven Schröder [d], Sundar Hengoju [a], Miriam A. Rosenbaum [a,b,e,*], Marc Thilo Figge [b,c,e,**]

[a] Bio Pilot Plant, Leibniz Institute for Natural Product Research and Infection Biology – Hans-Knöll-Institute HKI, Jena, Germany
[b] Institute of Microbiology, Faculty of Biological Sciences, Friedrich Schiller University, Jena, Germany
[c] Applied System Biology, Leibniz Institute for Natural Product Research and Infection Biology – Hans-Knöll-Institute HKI, Jena, Germany
[d] Functional Surfaces and Coatings, Fraunhofer Institute for Applied Optics and Precision Engineering IOF, Jena, Germany
[e] Cluster of Excellence Balance of the Microverse, Friedrich Schiller University, Jena, Germany

ARTICLE INFO

Keywords:
Droplet microfluidics
Angle-resolved light scattering
Deep learning
High-throughput
Rapid phenotypic antibiotic susceptibility testing

ABSTRACT

The progressive increase in microbial resistance to antibiotics is a global health threat that requires solutions for rapid and reliable determination of antibiotic susceptibility in order to select appropriate antibiotics and dosages prior to treatment. We have established a screening platform that enables the detection of cell growth after just a few cell divisions. Our methodological approach for a robust phenotypic antibiotic susceptibility testing is based on the innovative combination of three cutting-edge technologies: (i) a high-throughput microfluidic platform where individual bacterial cells are encapsulated in picoliter-sized droplets, (ii) a 2D angle-resolved light scattering sensor to perform label-free hourly screening of the droplets, and (iii) a computational image analysis approach based on convolutional neural networks to evaluate the dynamics of microbial growth in droplets. For the gram-positive *Staphylococcus aureus* and gram-negative *Escherichia coli,* we demonstrate that microbial growth in droplets can be successfully detected within one to two hours. Furthermore, the potential of this platform for rapid phenotypic antibiotic susceptibility testing is demonstrated as a proof-of-concept with the clinically relevant bacterium *S. aureus* under various concentrations of the antibiotic tetracycline. Notably, we reach a robust phenotypic decision regarding the sensitivity to this antibiotic within two hours.

1. Introduction

Antibiotic resistance has emerged as a pressing global health threat, undermining the effectiveness of antimicrobial treatments, and significantly impacting patient's mortality. A recent report stated that in 2019 alone, 1.27 million people lost their lives due to multidrug resistant bacteria [1]. This spread has not only been accelerated by the overuse and misuse of antibiotics, but also by the untargeted application of broad-spectrum antibiotics in the absence of specific sensitivity profiles of the pathogen in both human and animal healthcare [2,3].

To combat the escalating crisis, timely detection of antibiotic resistances is necessary to minimize the use of ineffective or broad-spectrum antibiotics. Many different antibiotic susceptibility tests (AST) have been developed to address this problem [4–6]. Techniques such as multiplex polymerase chain reaction for identifying resistance gene markers and mass spectrometry for detecting metabolites from resistance genes [7,8] provide results within two hours. However, only known resistance patterns can be detected in this way [9,10]. Phenotypic methods, in contrast, rely on the actual response of microorganisms to specific antibiotics. Growth-independent phenotypic methods can analyze cell behavior when exposed to antibiotics to determine sensitivity [11–13]. These methods provide results within 30 minutes to

* Corresponding author at: Bio Pilot Plant, Leibniz Institute for Natural Product Research and Infection Biology – Hans-Knöll-Institute HKI, Jena, Germany.
** Corresponding author at: Applied System Biology, Leibniz Institute for Natural Product Research and Infection Biology – Hans-Knöll-Institute HKI, Jena, Germany.
E-mail addresses: miriam.rosenbaum@leibniz-hki.de (M.A. Rosenbaum), thilo.figge@leibniz-hki.de (M.T. Figge).
[1] These authors contributed equally to this work.

https://doi.org/10.1016/j.snb.2024.136866
Received 26 June 2024; Received in revised form 9 September 2024; Accepted 28 October 2024
Available online 29 October 2024

two hours, and they do not rely on prior knowledge of resistance patterns. However, to date, growth-dependent cultivation methods, which assess actual microbial growth or inhibition in the presence of various antibiotics, are still the gold standard in clinical laboratories. Such techniques include disk diffusion [14], broth microdilution [15], and automated AST systems, such as VITEK® 2 (bioMérieux) [16,17]. The downside of these methods is the relatively long incubation time ranging from 8 to 20 hours [16–18] and, hence, a delay in the selection of appropriate antibiotics. These tests, therefore, cannot provide results in time for initial treatment decisions. Consequently, growth-dependent AST methods utilizing microfluidics have been proposed in recent years to improve measurement speed and multiplexing [19–25].

Apart from parallelization and multiplexing, droplet microfluidics offers several advantages over standard procedures in the context of rapid phenotypic detection, such as reduced reagent volumes and enhanced automation [26]. It enables high-throughput by parallel testing of multiple types and concentrations of antibiotics on microbial or patient samples. Several thousand monodisperse droplets can be generated every second, allowing the efficient generation of large amounts of miniaturized bioreactors [27]. Additionally, each droplet can encapsulate a single cell, resulting in droplet readouts derived from monoclonal populations [28]. This enables a much more defined insight into population behaviors, e.g. regarding heteroresistance towards antibiotics, than with bulk cultivation methods [29].

In most cases, growth detection in microfluidic platforms involves microscopy-based methods, which can provide high resolution images, however, they are restricted to observing a single focal plane at a time and therefore are either limited by throughput [30–32] or sensitivity [33]. An alternative approach relies on the detection of light scattering: The interaction of electromagnetic radiation with material gives rise to electromagnetic scattering which contains information about the illuminated object. Investigating cells via their light scattering is inherently label-free and is compatible with various bacterial species, ensuring a high-throughput capability. The intensity of the scattered light is directly correlated with the quantity of the cells. Several reports used light scattering at a single angle to detect cell growth in droplets when exposed to antibiotics. Without the presence of an antibiotic, growth could already be detected after five hours of incubation [34]. However, conclusions about antibiotic susceptibility were made after a relatively long incubation time of 16 to 24 hours [34–36]. More information can be deduced from the angle-resolved scattered light, because the light intensity distribution at different scattering angles relates to the structural and optical characteristics of the illuminated object. This approach is well established in the field of optical technologies for analyzing even subnanometer roughness and submicrometer defects on smooth surfaces (e. g. mirrors) [37–41]. Yu *et al.* have used this approach for a microbiological application and analyzed angle-resolved light scattering distributions to detect λ-bacteriophage infection of *E. coli* [42]. Recently, Munser *et al.* showed a 2D angle-resolved scattering (ARS) measurement and analysis approach to differentiate between various low bacteria cell concentrations and cell types in small static liquid volumes [43]. Besides the high sensitivity towards the smallest features, the strength of the approach lies in the robustness towards small deviations of object locations, e.g. by cell movement within the illumination spot. This combination makes it an ideal analysis tool for the detection of low cell concentrations in microfluidic droplets in flow, i.e. for rapid single-cell based phenotypic AST.

The data resulting from 2D ARS imaging are highly complex. Light scattering images show an intensity distribution dependent on the polar and azimuthal angular directions related to the sample structures, rather than an image of the object itself. Several models exist to describe the relations and theoretical light scattering behavior of idealized features, such as the Mie scattering theory for homogenous spheres, or the Rayleigh-Gans-approximation for small particles [44,45]. Modeling of real structures, however, becomes increasingly complex, especially with regard to the additional structural complexity added by the surrounding droplets. Therefore, the approach pursued here is to evaluate the data directly with regard to characteristic features of the sample (i.e., cell concentration). This requires specialized new approaches to derive quantitative information. Deep learning methods have risen as a popular approach for analyzing high throughput image data [46,47]. The most common model for deep learning based analysis of images are variations of convolutional neural networks (CNNs) [48]. In microscopy, CNNs have been applied on various scales, from tissue histology segments [49] and live cell imaging [50] to electron microscopy [51], where they can be used to segment specific structures or classify the image as a whole. CNNs have also been used to analyze different scattering modalities, including depth-resolved angular light scattering [52] and small-angle scattering [53]. Traditional analysis methods, including some machine learning models like Random Forest, for images and spectroscopic data require preselected, hand-crafted features while CNNs extract and weight features based on data during training [54]. Our workflow combined unsupervised and supervised CNNs followed by statistical analysis, which provided many more possibilities to detect differences in the 2D ARS pattern besides frequency. We have tailored our experimental and analytical workflow for *E. coli* and *S. aureus*, demonstrating our platform's versatility by handling different bacterial species. The rapid detection capability is a significant improvement over traditional methods, reducing the waiting time for results to under two hours, offering a new strategy for faster clinical decision-making.

2. Materials and Methods

2.1. Microorganisms and culture conditions

S. aureus ST033804 and *E. coli* ST036325 both from the Jena Microbial Resource Collection were used in this study. Pre-cultures were cultivated overnight at 37°C and 200 rpm. The main culture with an optical density at 600 nm (OD) of 0.1 (BioPhotometer, Eppendorf) was prepared 2–3 hours before droplet generation and incubated further. An OD of 0.003 was used for growth experiments to achieve single-cell encapsulation. Lysogeny broth medium was used for cultivation of both organisms. Tetracycline (Sigma, TET) in 70 % ethanol was added right before droplet generation for selected experiments to result in final TET concentrations of 0.03, 0.1, or 0.5 μg mL^{-1}.

2.2. Microfluidic chip fabrication

Microfluidic chips were designed in-house using AutoCAD 2021 (Autodesk Corp) and polydimethylsiloxane (PDMS) soft lithography was used to form chips from the wafers as described by Tovar *et al.* [55].

2.3. Droplet generation and incubation

Droplets were generated by using an OB-1 pressure pump (Elveflow) and polytetrafluoroethylene (PTFE) tubing (d_o/d_i = 1/16"/0.5 mm). A flow-focusing structure with a nozzle size of 50 μm (Figure S1) as well as Novec HFE7500 oil with 0.4 % (v/v) FluoSurf (Emulseo) was used. The collected droplets (~150 pL) were either directly transferred to the ARS imaging platform or incubated at 37 °C for 1–5 hours.

2.4. ARS and microscopic imaging

The ARS sensor setup is based on the sensor described by Munser *et al.* with some changes and additions (Figure S1a) [43,56]. Droplets were reinjected into a microfluidic chip which was placed in the laser path of the ARS sensor (Figure S1b). The flow speed was adapted, so that ~20–60 droplets per second passed through the imaging region. A triggering setup as described by Zang *et al.* was used [57].

For acquiring brightfield images of flowing droplets, a fluorescence-based detection and triggering system was utilized with a previously published setup (Section Supplementary Information SI1) [35]. For

static imaging an inverted microscope (Axio Observer Z1, Zeiss) with a magnification of 40x was used.

2.5. Microcultivation experiments

A two-fold dilutions series starting with an active concentration of 0.5 μg mL^{-1} of TET was prepared and mixed with *S. aureus* cells to receive a concentration of OD 0.1. 200 μL of each dilution step (n = 3) was pipetted into a 96-well plate (Greiner Bio-One) and sealed with foil. The change in biomass was analyzed with a BioLector® I microcultivation system (m2p-labs) through scattered light measurements at 37 °C and 600 rpm shaking. A gain of 40 and humidity control were used. The amplitude at five hours was used to determine growth. The growth condition without TET was set to 100 % growth.

2.6. Deep learning models and statistical analysis

An unsupervised deep learning approach was adopted for the assessment of ideal exposure time for ARS imaging (800, 1500 and 2000 μs) (Section SI2.1 and Figure S2). A supervised deep learning CNN model, EfficientNetV2-M [58], was trained to identify falsely triggered images and remove them (Section SI2.2).

For the OD estimation, two separate CNN based regression models were trained for the two organisms. For the regression models, a pre-trained EfficientNetV2-XL [58] architecture, pre-trained on the ImageNet21K dataset, was utilized as the foundation. Labelled ARS images from the dilution series were used for training (*S. aureus*: 75,537 and *E. coli*: 50,772 images). Falsely triggered images from the growth experiments were removed and the remaining images were analyzed with the regression models trained on the dilution series (Section SI2.3). The analysis of the TET susceptibility experiments was conducted in the same manner as the other growth experiments.

To determine significant change of growth based on the predicted ODs, a statistical model was developed that analyzes the percentage of droplets with growth and the amount of growth (Section SI3).

3. Results and Discussion

3.1. Overview of the high throughput phenotypic AST platform

We have developed an analytical platform that can already detect a few bacterial cell divisions in flowing picoliter-sized droplets, which enables rapid phenotypic AST. In our established workflow, single-cells were encapsulated in picoliter-sized droplets, incubated at optimal growth conditions for defined times and reinjected into a microfluidic chip for analysis. The droplets flowed through a laser beam, which caused the laser light to scatter. The recording of a 2D angle-resolved scattering (ARS) image with a dimension of 3200 × 2200 pixels was triggered [57] whenever the droplet was in the center of the beam (Fig. 1**a i-ii**, S2)**.** The light scattering pattern and intensity is dependent on the cell concentration and morphology. The captured ARS images were analyzed with a pre-trained CNN, based on the EfficientNetV2-XL [58] architecture, which predicted the OD of a droplet (Fig. 1**a iii).** If the cells were encapsulated together with an antibiotic, the susceptibility towards that antibiotic was determined relative to control growth.

The encapsulated cells were screened with the ARS sensor while flowing through a microfluidic channel. Therefore, the impact of the movement and encapsulation on the scattering pattern at different cell concentrations must be considered. Exemplary scattering images of normalized angle-dependent intensities are shown in Fig. 1**b**. The beam transmitted directly through the sample was blocked by a beam stop, resulting in the circular shaded region in the center of the images. Empty droplets mainly scattered light into low angles (close to the center of the image), while the presence of cells also caused light scattering at higher angles. Droplets with very low cell concentrations caused a clear ring pattern, while higher concentrations resulted in speckled rings. The

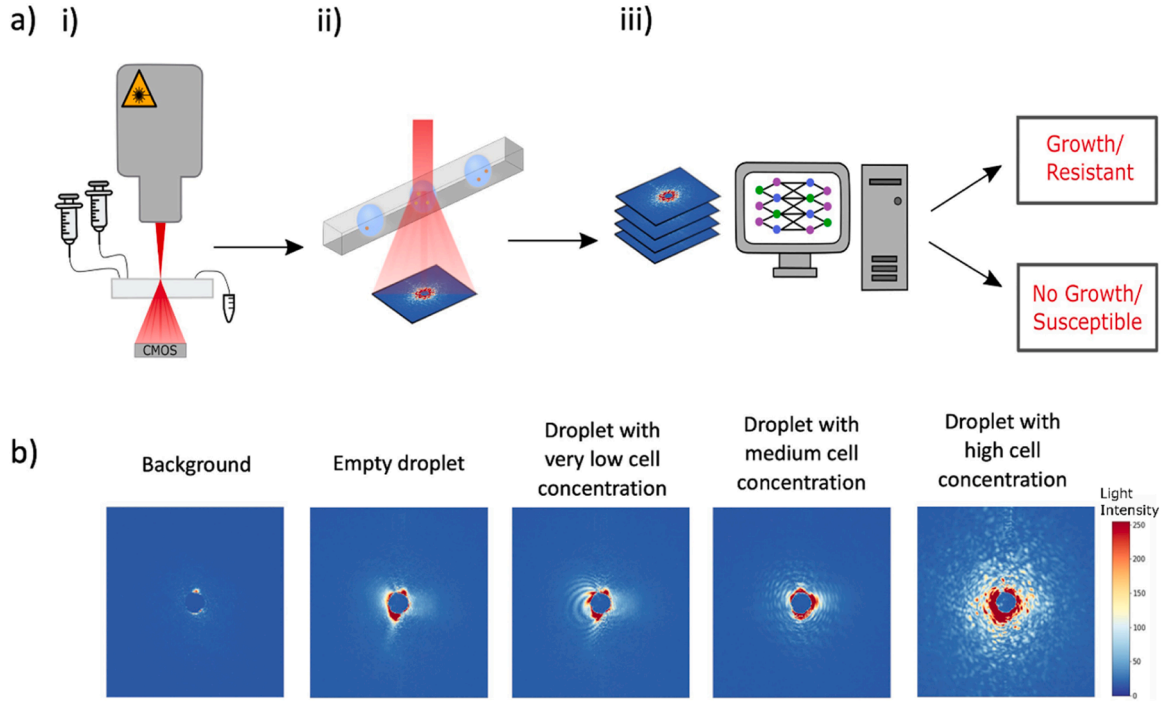

Fig. 1. : a) Schematic of the workflow. i) Laser-based sensor for angle-resolved scattered light (ARS) imaging of picoliter-sized droplets in a microfluidic chip. ii) ARS imaging of droplets flowing through a microfluidic channel. iii) The ARS images are analyzed with a convolutional neural network (CNN). A predicted OD is given as output and therefore it can be determined whether the cells inside of the droplets grew or not. When an antibiotic is present, the sensitivity of the strain towards that antibiotic can be determined. b) Exemplary ARS images are shown. The light that is directly transmitted is blocked (dark blue spot in the image center). The droplet itself causes a high light intensity around the center of the image (at small angles). For the sake of simplicity, the angular grid is not shown. Droplets with low cell concentrations caused clear rings. Higher cell concentrations caused speckled rings. The more cells the higher the caused speckle density.

higher the cell concentration, the higher the speckle density. The droplet movement caused a small information loss due to motion blurriness at small angles, which increased with higher exposure times. An exposure time of 800 µs resulted in a clear visual separation between different cell concentrations and additionally enabled fast image acquisition and caused low motion blurriness (Section SI2.1, Figure S2). Longer exposure times further increased the separation of clusters, but at the cost of less information at low scatter angles (Figure S2). Therefore, 800 µs was deemed to be a sufficient exposure time.

3.2. Detection of defined cell concentrations

In order to derive a cell concentration from an ARS image, droplet populations with different defined mean ODs at 600 nm (0, 0.01, 0.1, 0.5, 1) of *S. aureus* and *E. coli* were generated (example bright field images in Figure S3) and screened with the ARS imaging platform as training data sets. We determined by manual cell counting that the abovementioned ODs translate to on average 0, 1, 10, 60 and 120 cells per droplet, respectively (Figure S4). ARS images were acquired with 25 Hz, resulting in 1500 imaged droplets per minute. For image analysis, an EfficientNetV2-M[53] deep learning model was first trained on 10,933 manually-preassigned ARS images to automatically remove images in which the droplets were not in the center of the laser beam (Figure S5). Between 0 % and 4 % of the images per experiment were affected across different droplet flow rates (Figure S6). The two organisms have different cell morphologies (cocci shaped *S. aureus* and rod-shaped *E. coli*) that directly impact the ARS patterns (Section SI2.4, Figure S7). Hence, two separate supervised CNN based regression models were trained for each organism for predicting ODs (training images - *S. aureus*: 42,300, *E. coli*: 32,493) (Fig. 2**a**). The regression models were trained to provide precise continuous OD values, offering a more nuanced understanding compared to categorical classifications. Although the actual number of cells per droplet varied due to the stochastic nature of the encapsulation of the dilution in droplet, each droplet used for training was given the mean OD of the solution as a label. The training of the regression model will therefore be limited by the fact that many of the droplets labelled OD 0.01 are actually empty. The box plot representation of results for *S. aureus* **(**Fig. 2**b i)** reveals that the model predictions closely aligned with the actual OD values. The spread of the predicted ODs is caused by the random number of cells that are encapsulated in each droplet from a given cell concentration. The variance in predicted OD was therefore a combination of actual variance of cell concentrations in the test set and the approximate labelling of every ARS image used for training. In the case of *E. coli* (Fig. 2**b ii**), the regression model exhibits a similar level of precision in OD predictions, with the interquartile range of the box plots indicating consistent

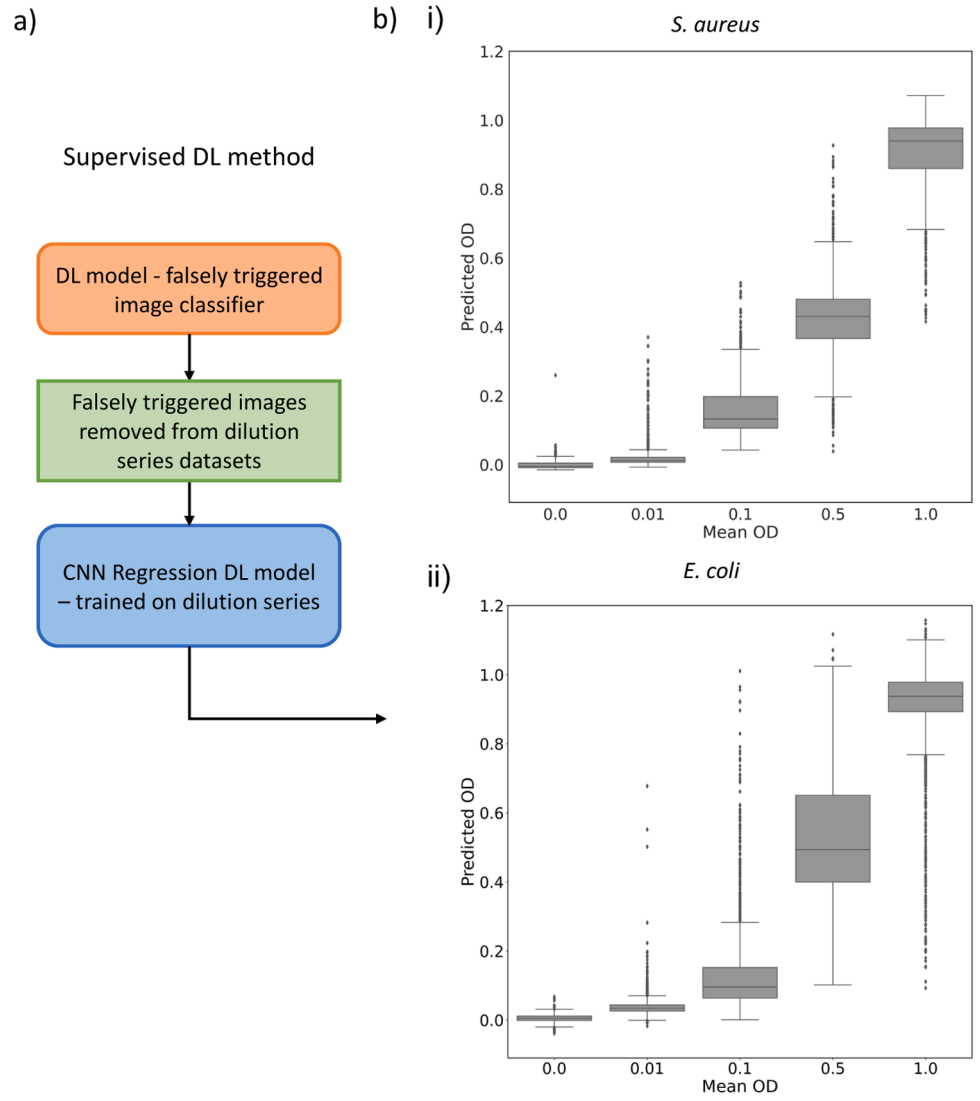

Fig. 2. : a) Overview of the analysis steps of ARS images. b) Predicted OD distributions versus mean ODs of five different droplet populations with i) *S. aureus* and ii) *E. coli* cells.

performance across the different OD values. Thus, based on the predicted distributions of *S. aureus* and *E. coli*, the ODs and thus the cell concentrations of bacteria in droplets can be inferred from ARS images, regardless of cell morphology. These predictions of the deep learning models were very fast, with an analysis speed of 19.2 frames per second (fps) with a single graphics processing unit (40 GB NVIDIA A100 GPU). This enables a swift analysis of very large datasets that are common in high-throughput experimentations.

3.3. *S. aureus and E. coli growth detected within two hours*

As a next step, the detection time window for bacterial growth in droplets was determined. For this, single cells of either *S. aureus* (Fig. 3**a-c**, S8a) or *E. coli* (Fig. 4**a-c**, S8b) were encapsulated in droplets and incubated at 37 °C for five hours. The majority of droplets remain empty when targeting single cell inoculation. ARS images of a few thousand droplets were captured hourly and then analyzed with the previously trained regression model for the respective organism (Figs. 3a, 4a). The number of droplets with predicted low OD values (0–0.15) were predominant (Figure S9), which was attributed to the majority of droplets being empty (estimated 90 – 95 %). This time, the mode of the OD histogram is not located at zero, as we saw in the dilution series histogram at OD 0 (Figure S10). The reason is most likely small differences between individual experiments, which makes the discrimination between empty droplets and droplets containing only a few cells uncertain. Therefore, we took a cautious approach in this study and focused on growth above a detection threshold, which was decided to be the 99.9 percentile at time t = 0 and only show growth distributions with OD > 0.15 in the figures.

Figs. 3b and 4b show the Kernel Density Estimation (KDE) [59] of the predicted OD distributions above the threshold for the two evaluated bacteria. The KDEs were normalized so that the area under each curve is equal to the proportion of droplets that exhibit growth, $\pi_{1,t,c}$ (Section SI3, Equation S1**)**. For *S. aureus*, some growth was already visible at one hour, which becomes more evident from two hours onwards. The number of droplets exhibiting growth and the associated OD values showed a progressive increase with time. At four hours, OD values reached up to OD ≈ 1, which was the upper limit of the regression model's training range. Consequently, at five hours, the OD peak-values plateaued slightly above OD = 1.1 (Fig. 3b, S11).

However, as can be seen from the individual graph lines of the replicates, the biological variability should be accounted for in the robust detection of growth differences. To be able to incorporate both the proportion of droplets that exhibits growth at all, as well as the amount of growth in those droplets we developed a statistical model (Section SI3, Equation S1). By fitting this model to individual experiments, we can determine if an experimental condition exhibits significantly more or less growth compared to another condition, while we consider the biological growth variability between replicates of the same growth conditions. To determine the range of variability of identical growth conditions, we compared all three independent experimental replicates of *S. aureus* growth over five hours. We then saw that the range of $p\left(G_i(\hat{t}) > G_j(\hat{t})\right)$ was

$$0.22 > p\left(G_i(\hat{t}) > G_j(\hat{t})\right) < 0.78 \tag{1}$$

for all permutations of $i, j \in [1, 2, 3]$ for any time $\hat{t} \in [0, 1, 2, 3, 4, 5]$. This is visualized in Figure S12, and this range gives us a natural limit to what we can expect from inter-experimental variation. We found that $p(G_1(\hat{t} = 1) > G_3(\hat{t} = 1)) = 0.22$ was the most extreme value and, due to the interchangeability of the notations $G_i(\hat{t})$ and $G_j(\hat{t})$, the upper limit we could expect was $p(G_3(\hat{t} = 1) > G_1(\hat{t} = 1)) = 1 - 0.22 = 0.78$. Any comparison of a condition against another or comparing the different timepoints from a single experimental condition where the difference in growth is outside the range of Eq. 1 will be considered significant. With this model, the timepoint of a significant change of growth against t = 0 can be determined. Hence, for *S. aureus,* experiment 3 showed significant growth already after one hour of incubation ($p(G_3(t = 1) > G_3(t = 0)) \approx 0.87$), while a significant growth level was reached after two hours ($p(G_1(t = 2) > G_1(t = 0)) \approx 0.94$ and $p(G_2(t = 2) > G_2(t = 0)) \approx 0.95$) for the other two experiments (Fig. 3c). A similar trend was observed for *E. coli* with growth becoming more pronounced and the range of OD values broadening as the incubation time increased (Fig. 4b, S13). All three replicates with *E. coli*, showed significant growth levels already after one hour of incubation with $p(G_i(t = 1) > G_i(t = 0)) \approx 0.95\ \forall i \in [1, 2, 3]$ (Fig. 4c). This means, that a single measurement after one hour for *E. coli* and after two hours for *S. aureus* is sufficient to detect growth inside droplets.

3.4. *Sensitivity comparison of ARS imaging platform against in-flow brightfield imaging*

To demonstrate the advantage of ARS imaging over classical microscopy, we imaged the droplets from experiment 3 of Fig. 3b in parallel in flow using brightfield imaging (Section SI1, Figure S14). The results of the growth analysis from ARS and brightfield imaging were plotted separately (Fig. 5**a**, **b**). A continuous increase in growth can be seen with both imaging techniques, however, the increase is detected much faster with ARS imaging. This trend was also confirmed by the developed stochastic model: we detected growth already after one hour for experiment 3 using ARS, while with brightfield imaging of the same droplet population, significant growth was detected after three hours ($p(G_{BF}(t = 3) > G_{BF}(t = 0)) \approx 0.96$, Fig. 5**c**). Hence, the ARS imaging platform can detect growth two hours earlier than brightfield imaging of flowing droplets. This advantage is founded on two main reasons: Firstly, for the brightfield image, a relatively low magnification of 10x was used to capture the entire droplet in the field of imaging. Consequently, this lead to a comparably low resolution (Fig. 5**d**). Secondly, ARS imaging is not limited to one focal plane in contrast to brightfield imaging of moving droplets. Therefore, the entire droplet in the axial direction can be scanned for cell growth within microseconds.

3.5. *ARS imaging is applicable for rapid phenotypic antibiotic sensitivity testing*

To showcase the potential of the ARS platform for rapid phenotypic AST, proof-of-principle experiments to determine the effect of tetracycline (TET) on microbial growth were conducted. The organism *S. aureus* was used because it has significant clinical relevance as a leading cause of a wide range of infections, including skin and soft tissue infection, pneumonia, bloodstream infections, and surgical site infections [60,61]. Moreover, it is often exhibiting resistance to multiple antibiotics at once [62], making it difficult to pick an effective antibiotic without AST. TET is utilized in the treatment of a wide range of infections, including respiratory infections such as pneumonia, as well as infections of the skin, eyes, intestines, genitals, and urinary tract. It is also effective against infections transmitted by animals, such as tularemia, and is prescribed for certain types of food poisoning and anthrax in patients who are unable to receive penicillin [63]. Given the occurring antibiotic resistances, rapid AST is necessary for some of these infections [64,65]. Notably, there has been a rise in the identification of methicillin-resistant *S. aureus* strains that also exhibit resistance to tetracyclines [66,67].

Three concentrations of TET (0.03, 0.1, 0.5 μg mL^{-1}) were co-encapsulated with single *S. aureus* cells and imaged hourly. The percentage of detected non-empty droplets (Fig. 6**a**, S15) and their predicted ODs were calculated (Fig. 6**b**, S16). The higher the TET concentration, the fewer droplets with growth could be detected, and the ones with growth had in general a lower predicted OD than the control. While the predicted ODs at the lowest TET concentration were quite similar to the control, at 0.1 μg mL^{-1} TET growth was strongly

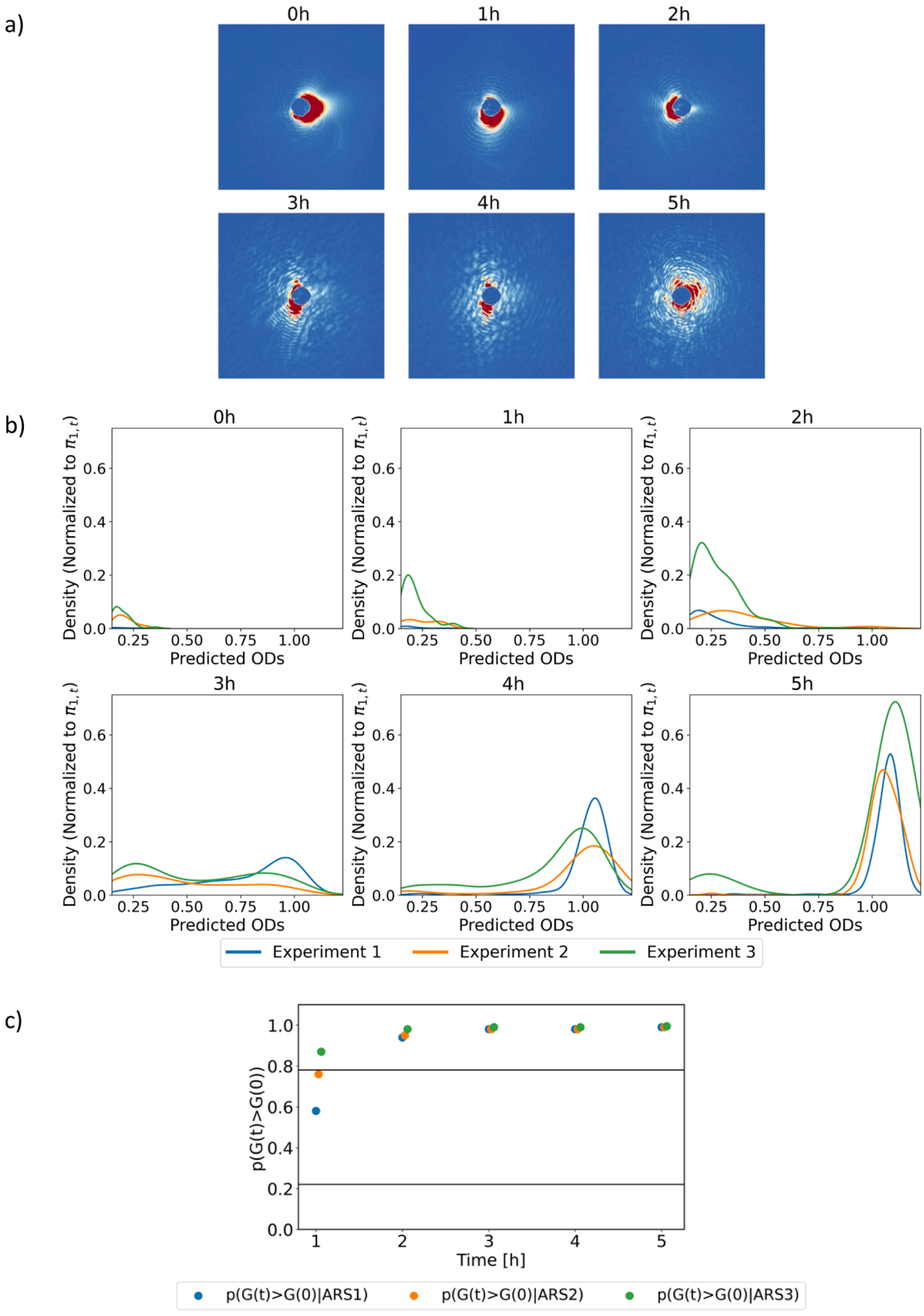

Fig. 3. : a) Exemplary images of growth experiment of *S. aureus* over five hours. Starting OD = 0.003. Droplets were incubated at 37 °C. b) Predicted ODs > 0.15 for every timepoint. c) Probability that *S. aureus* growth at timepoint t is larger than at $t = 0$. Significance limits are given by Eq. 1 and calculations were performed with Equations S1 and S2. To clearly show the data points, x-jitter was added in the plot. (p(G(t) > G(0)|ARS1) x-jitter = 0, (p(G(t) > G(0)|ARS2) x-jitter = 0.03, (p(G(t) > G(0)|ARS3) x-jitter = 0.06).

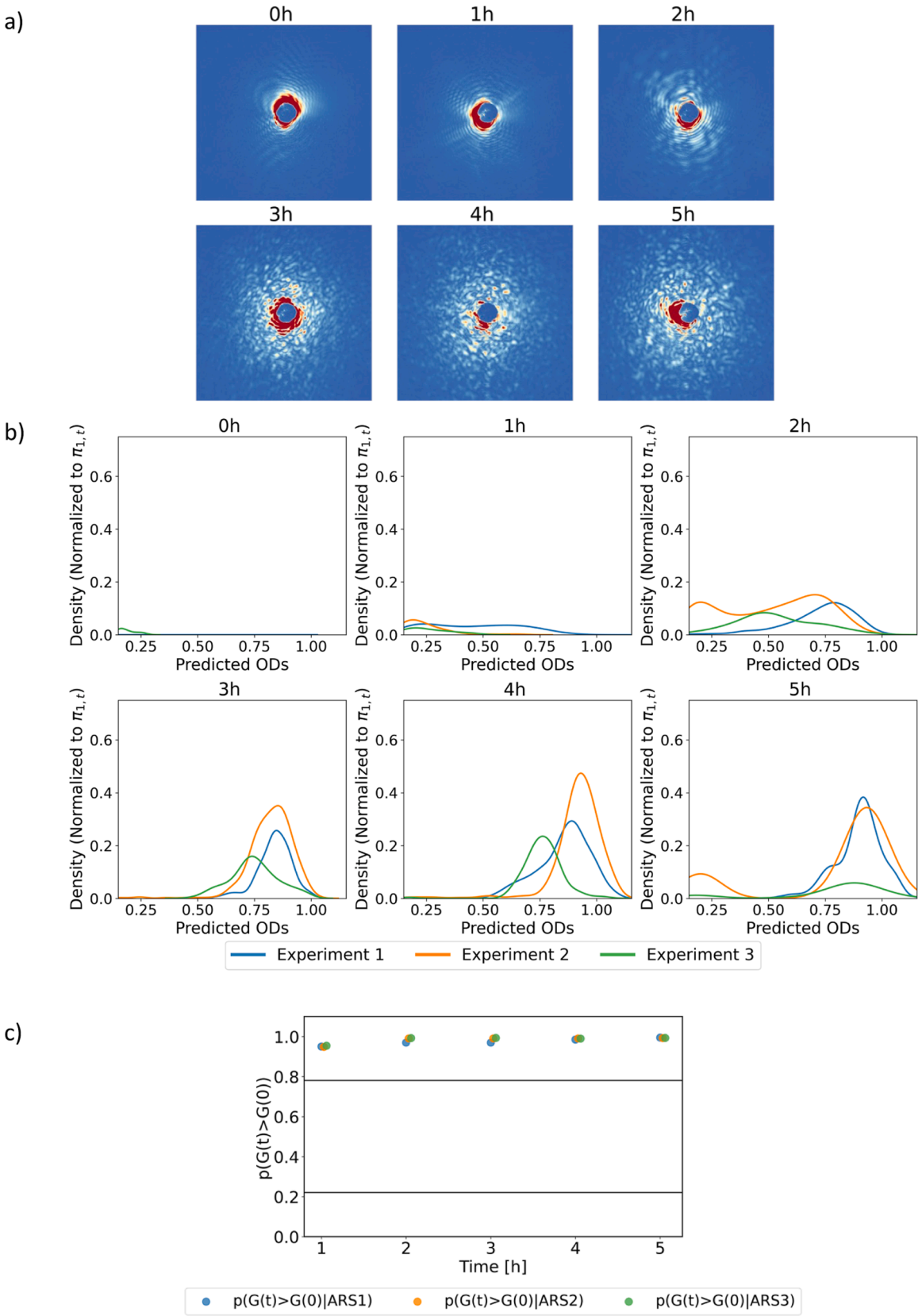

Fig. 4. : a) Exemplary images of growth experiment of *E. coli* over five hours. Starting OD = 0.003. Droplets were incubated at 37 °C. b) Predicted ODs > 0.15 for every timepoint. c) Probability that *E. coli* growth at timepoint t is larger than at $t = 0$. Significance limits are given by Eq. 1 and calculations were performed with Equations S1 and S2. To clearly show the data points, x-jitter was added in the plot. (p(G(t) > G(0)|ARS1) x-jitter = 0, (p(G(t) > G(0)|ARS2) x-jitter = 0.03, (p(G(t) > G(0)|ARS3) x-jitter = 0.06).

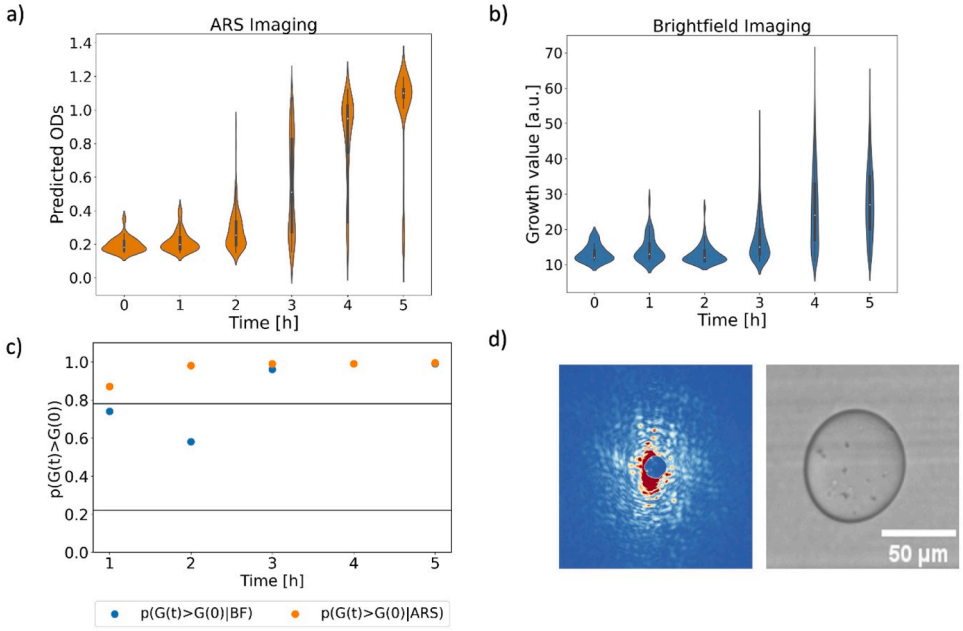

Fig. 5. : a) Violin plot of predicted OD at each timepoint of ARS imaging. Droplets with OD < 0.15 were not included for clarity as those empty droplets were the vast majority. b) same as in a) but instead of ARS images, brightfield images (10x) were taken in flow and analyzed in comparison. Droplets with growth value < 10 were not included for clarity as those empty droplets were the vast majority. c) Stochastic model of growth characteristics (Equations S1, S2) for ARS and brightfield images against characteristics at t = 0. d) Left: ARS image of a droplet with cells after three hours of incubation. Right: Brightfield image of a droplet with cells after three hours of incubation.

reduced, and at 0.5 µg mL^{-1} the level of growth was similar to its value at the initial timepoint t = 0. The stochastic model for determining a significant change of growth compared to the control yielded a significant growth reduction after two hours of incubation at 0.1 and 0.5 µg mL^{-1} TET ($p(G(t=2) > TET_{0.5}(t=2)) \approx 0.94$), and no significant change at 0.03 µg mL^{-1} (Fig. 6**c i-iii**). This means, that already after two hours of incubation, a conclusion about the sensitivity of the strain towards TET at each tested concentration can be drawn. The detection time of phenotypic antibiotic sensitivity could therefore be drastically reduced from 16 to 20 hours in classical cultivations like disc diffusion and roughly eight hours in high-throughput cultivations, e.g. VITEK® 2, down to one to two hours with our microfluidic ARS imaging and analysis platform.

Other phenotypic methods for AST also offer rapid results, sometimes even within two hours, such as Resistell, which measures the nanomotion of cells [11], and dropFAST, which utilizes resazurin for growth detection [68]. Pheno-molecular and molecular methods can reduce the time even further to within 15–30 min [69,70]. However, the advantage of our platform is that it is label-free and detects actual growth after one to two hours. This is the equivalent of just a few replication cycles, considering a doubling time of roughly 20 minutes for *E. coli* and *S. aureus* [71,72]. The difference in the detection time of both strains could be due to a longer lag-phase of *S. aureus*. The required incubation time for growth detection is primarily influenced by the growth kinetics of the organisms being tested. Organisms with slower growth rates will necessitate extended incubation periods. Nonetheless, the overall time required remains considerably shorter compared to standard techniques and other comparable high-throughput growth--based methods. It is important to note that many of the common pathogens, such as *S. aureus*, *E. coli*, *Campylobacter spp.*, exhibit rapid growth under optimal conditions [71–73]. Also, our developed platform does not rely on the use of any fluorescent dyes or probes, which might interfere with bacterial viability and does not require a special assay or probe preparation. Importantly, our method is flexible and applicable to different microbial strains. Only the deep learning models might have to be re-trained for morphological different bacteria. Compared to other growth-dependent and label-free methods, our platform is fast and has high-throughput capabilities.

Additionally, our assay delivered an antibiotic resistance profile on a single cell resolution. This enables also the evaluation of cell-to-cell variability of resistance and the detection of few resistant cells. At such short incubation times below two hours, a small number of resistant cells are expected to lie under the detection limit in bulk experiments. Through the single-cell analysis we see such heteroresistance, which has also been demonstrated by previous studies with single-cell AST in droplets [29,74].

In order to validate these results, micro-cultivations with various TET concentrations were conducted with an established assay. For this, a two-fold dilution series from 0.5 µg mL^{-1} TET was generated and the growth amount of *S. aureus* was analyzed after incubation. At 0.5 µg mL^{-1}, cells were fully inhibited, while at 0.1 µg mL^{-1}, a reduction of growth down to 39 % of the control was observed, and at 0.03 µg mL^{-1} no significant change in the growth behavior could be detected (Fig. 6**d**). The p-values of the student t-test of growth in regard to 0 µg mL^{-1} TET are 2.8 $\times 10^{-5}$ for 0.5 µg mL^{-1}, 9.5 $\times 10^{-4}$ for 0.1 µg mL^{-1} and 0.68 for 0.03 µg mL^{-1} TET, resulting in significant changes in growth with the two higher concentrations of TET. The results from the bulk cultivations are, therefore, in good agreement with the inhibition results from the ARS imaging platform.

4. Conclusion

In this study, we combined three cutting-edge technologies: (i) a high-throughput microfluidic platform where individual bacterial cells are encapsulated in picoliter-sized droplets, (ii) a 2D angle-resolved light scattering sensor to perform label-free imaging of the droplets, and (iii) a computational image analysis approach based on CNNs to monitor the dynamics of microbial growth in droplets. This approach allowed us to realize the high-throughput differentiation of various cell concentrations as well as the growth measurement of cell populations starting from a single cell. Growth could be reliably detected after one and two hours for *E. coli* and *S. aureus,* respectively. Thousands of droplets were

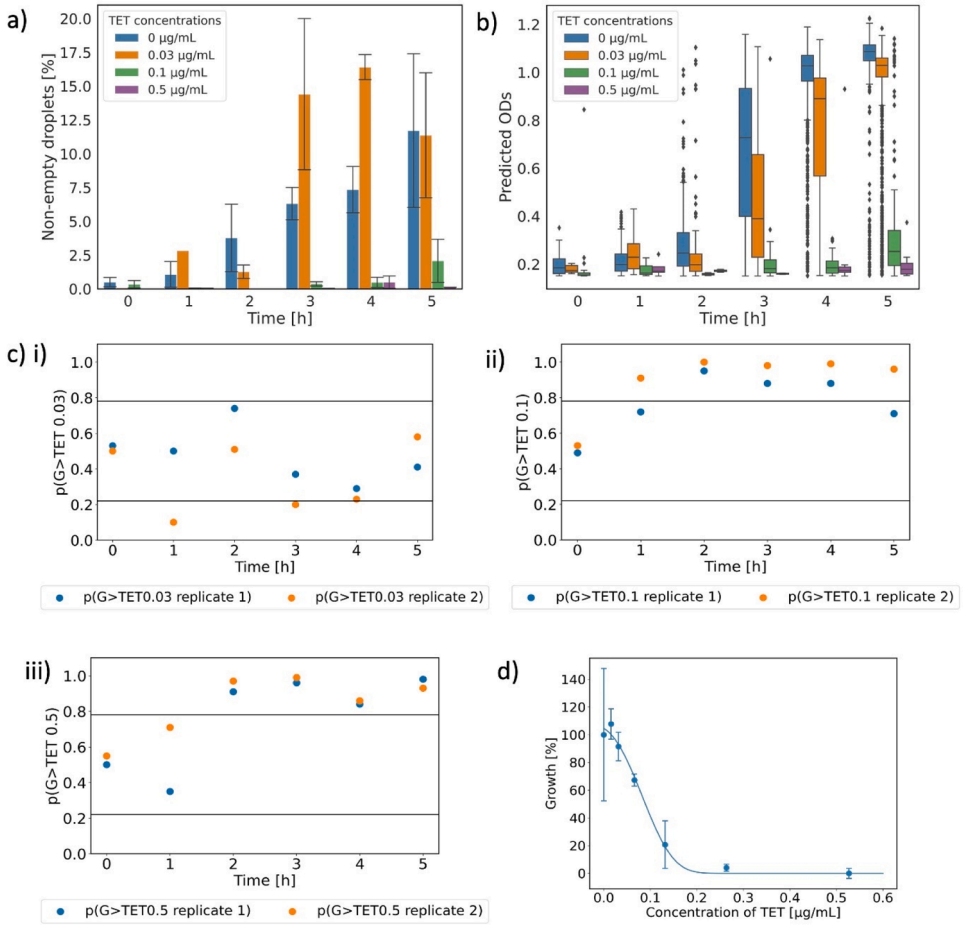

Fig. 6. : *S. aureus* cells (OD 0.003) were encapsulated with three concentrations of tetracycline (0.03, 0.1, 0.5 µg mL^{-1}) and incubated at 37 °C for five hours. ARS images were taken hourly. a) The percentage of non-empty (OD > 0.15) droplets were plotted over time in reference to the TET concentration. b) The predicted ODs of the non-empty droplets over time. c) Monte-Carlo sampling from the fitted stochastic model of growth comparing the different antibiotic concentrations against the three control growth experiments. i-iii) The probability for each TET experiment is averaged against the three control experiments. d) Microcultivation experiment of *S. aureus* cells with various concentrations of TET as validation of our ARS platform. A Gompertz function was fitted.

imaged within less than ten minutes and analyzed with deep learning supported CNNs within a few minutes. Our results reveal that ARS imaging is more sensitive than microscopic inspection of droplets in flow, which in particular is due to the fact that ARS imaging is not restricted to imaging a single focal plane but rather illuminates the entire droplet at once. We, therefore, conclude that this high-throughput, sensitive and label-free detection method has the capability for rapid single-cell AST. This was demonstrated in a proof-of-concept study for the clinically relevant organism *S. aureus* and three concentrations of tetracycline. The sensitivity towards the antibiotic concentrations could be reliably determined after two hours of incubation. The integration of deep learning into our high-throughput, label-free detection method marks a significant advancement in microbial diagnostics and AST. Deep learning, particularly with CNNs, allows for rapid and efficient analysis of complex ARS image data. Once these models are trained, they enable swift and accurate interpretations, which are essential for timely clinical decision-making.

For this platform to be even more potent for rapid AST, multiplexing of multiple different antibiotics needs to be implemented [75,76]. Also, validation of this platform by testing bacterial strains with unknown resistance patterns as well as different antibiotics will be a next step. In addition, implementation of sample preparation steps, such as cell separation and adjustment of cell concentration prior to encapsulation will be crucial for rapid AST from complex biological samples in clinical applications. Beyond AST, the methodology presented in this proof-of-concept study is also able to retrieve information on cell morphology [43]. This could potentially be used to simultaneously identify and follow the growth of morphologically different members of a microbial mixed culture. This would also include the development of an array of different CNNs that are trained to determine the growth of several groups of microbes with different morphologies and cell arrangements. Another important application is the detection of rare and slow-growing microorganisms from environmental samples in microfluidic droplets [77]. These rare microbes are often very slow-growing so that growth is overlooked when empty droplets are separated from droplets with growth by classical microscopic analysis. With this platform, it would be possible to specifically target the slow-growing microbial cells. Overall, our platform can be used for multiple microbial and biomedical applications such as minimal inhibitory concentration determination, rapid single-cell based AST and screening for growth or morphological heterogeneity within bacterial populations.

CRediT authorship contribution statement

Martina Graf: Writing – review & editing, Writing – original draft, Visualization, Methodology, Investigation, Formal analysis. **Arjun Sakar:** Writing – review & editing, Writing – original draft, Visualization, Software, Methodology, Formal analysis. **Carl-Magnus Svensson:** Writing – review & editing, Writing – original draft, Visualization, Methodology, Formal analysis. **Anne-Sophie Munser:** Writing – review & editing, Methodology. **Sven Schröder:** Writing – review & editing, Supervision. **Sundar Hengoju:** Writing – review & editing,

Investigation. **Miriam Rosenbaum:** Writing – review & editing, Supervision, Resources, Funding acquisition, Conceptualization. **Marc Thilo Figge:** Writing – review & editing, Supervision, Resources, Funding acquisition, Conceptualization.

Declaration of Competing Interest

The authors declare the following financial interests/personal relationships which may be considered as potential competing interests. Martina Graf has patent Optische Messvorrichtung, Messverfahren und Auswerteverfahren pending to Leibniz HKI and Fraunhofer IOF. Arjun Sakar has patent Optische Messvorrichtung, Messverfahren und Auswerteverfahren pending to Leibniz HKI and Fraunhofer IOF. Carl-Magnus Svensson has patent Optische Messvorrichtung, Messverfahren und Auswerteverfahren pending to Leibniz HKI and Fraunhofer IOF. Anne-Sophie Munser has patent Optische Messvorrichtung, Messverfahren und Auswerteverfahren pending to Leibniz HKI and Fraunhofer IOF. Sven Schroeder has patent Optische Messvorrichtung, Messverfahren und Auswerteverfahren pending to Leibniz HKI and Fraunhofer IOF. Marc Thilo Figge has patent Optische Messvorrichtung, Messverfahren und Auswerteverfahren pending to Leibniz HKI and Fraunhofer IOF. Miriam A. Rosenbaum has patent Optische Messvorrichtung, Messverfahren und Auswerteverfahren pending to Leibniz HKI and Fraunhofer IOF. If there are other authors, they declare that they have no known competing financial interests or personal relationships that could have appeared to influence the work reported in this paper.

Acknowledgements

M.G. and A.S. contributed equally to this work as shared first authors. M.A.R. and M.T.F. contributed equally to this work as shared senior authors. This work was supported by the InfectoGnostics Research Campus 13GW0456B (Project ADA) through the German Federal Ministry of Education and Research, the Thuringian Ministry of Economics, Science and Digital Society and the European Regional Development Fund as well as the Leibniz ScienceCampus InfectoOptics (project VersaDrop) and the project “Leistungszentrum Photonik Imaging Labs” funded by the Thuringian Ministry of Economy, Science and Digital Society. Financial support was also given by the German Federal Ministry of Education and Research within the funding program Photonics Research Germany, Project Leibniz Center for Photonics in Infection Research, subprojects LPI-BT2 and LPI-BT3, contract numbers 13N15705 and 13N15709. The LPI initiated by Leibniz-IPHT, Leibniz-HKI, UKJ and FSU Jena is part of the BMBF national roadmap for research infrastructures. M.A.R. and M.T.F. also acknowledge funding by the Deutsche Forschungsgemeinschaft (DFG, German Research Foundation) under Germanys Excellence Strategy – EXC 2051 – Project-ID 390713860.

Appendix A. Supporting information

Supplementary data associated with this article can be found in the online version at doi:10.1016/j.snb.2024.136866.

Data availability

Data will be made available on request.

References

[1] Antimicrobial Resistance Collaborators, Global burden of bacterial antimicrobial resistance in 2019: a systematic analysis, Lancet 399 (2022) 629–655.
[2] J.E.J. McGowan, Antimicrobial resistance in hospital organisms and its relation to antibiotic use, Rev. Infect. Dis. 5 (1983) 1033–1048.
[3] V. Ćupić, S. Dobrić, B. Antonijević, S. Čelebićanin, The significance of rational use of drugs in veterinary medicine for food safety, Tehnol. mesa 52 (2011) 74–79.
[4] M. Ramzan, et al., Detection of antimicrobial resistance (AMR) and antimicrobial susceptibility testing (AST) using advanced spectroscopic techniques: A review, TrAC Trends Anal. Chem. 172 (2024) 117562.
[5] A. van Belkum, et al., Innovative and rapid antimicrobial susceptibility testing systems, Nat. Rev. Microbiol. 18 (2020) 299–311.
[6] E.C. Reynoso, S. Laschi, I. Palchetti, E. Torres, Advances in antimicrobial resistance monitoring using sensors and biosensors: a review, Chemosensors 9 (2021) 232.
[7] Y. Charretier, J. Schrenzel, Mass spectrometry methods for predicting antibiotic resistance, Proteom. - Clin. Appl. 10 (2016) 964–981.
[8] M. Welker, A. van Belkum, One system for All: is mass spectrometry a future alternative for conventional antibiotic susceptibility testing? Front. Microbiol. 10 (2019) 2711.
[9] M. Tato, et al., Carbapenem heteroresistance in VIM-1-producing Klebsiella pneumoniae isolates belonging to the same clone: Consequences for routine susceptibility testing, J. Clin. Microbiol. 48 (2010) 4089–4093.
[10] H. Rasheed, et al., Discrepancies between phenotypic and genotypic identification methods of antibiotic resistant genes harboring Staphylococcus aureus, Microb. Pathog. 184 (2023) 106342.
[11] A. Sturm, et al., Accurate and rapid antibiotic susceptibility testing using a machine learning-assisted nanomotion technology platform, Nat. Commun. 15 (2024) 2037.
[12] Y.-L. Chiang, et al., Innovative antimicrobial susceptibility testing method using surface plasmon resonance, Biosens. Bioelectron. 24 (2009) 1905–1910.
[13] A.M. Kaushik, et al., Droplet-based single-cell measurements of 16S rRNA enable integrated bacteria identification and pheno-molecular antimicrobial susceptibility testing from clinical samples in 30 min, Adv. Sci. 8 (2021) 1–14.
[14] A.W. Bauer, W.M. Kirby, J.C. Sherris, M. Turck, Antibiotic susceptibility testing by a standardized single disk method, Tech. Bull. Regist. Med. Technol. 36 (1966) 49–52.
[15] T.L. Gavan, M.A. Town, A microdilution method for antibiotic susceptibility testing: an evaluation, Am. J. Clin. Pathol. 53 (1970) 880–885.
[16] H. Leonard, R. Colodner, S. Halachmi, E. Segal, Recent advances in the race to design a rapid diagnostic test for antimicrobial resistance, ACS Sens. 3 (2018) 2202–2217.
[17] Z.A. Khan, M.F. Siddiqui, S. Park, Current and emerging methods of antibiotic susceptibility testing, Diagnostics 9 (2019) 49.
[18] E. Matuschek, D.F.J. Brown, G. Kahlmeter, Development of the EUCAST disk diffusion antimicrobial susceptibility testing method and its implementation in routine microbiology laboratories, Clin. Microbiol. Infect. 20 (2014) O255–O266.
[19] R.K. Shanmugakani, et al., Current state of the art in rapid diagnostics for antimicrobial resistance, Lab Chip 20 (2020) 2607–2625.
[20] G. Maugeri, I. Lychko, R. Sobral, A.C.A. Roque, Identification and antibiotic-susceptibility profiling of infectious bacterial agents: a review of current and future trends, Biotechnol. J. 14 (2019) 1–31.
[21] X. Jiang, et al., Accurate prediction of antimicrobial susceptibility for point-of-care testing of urine in less than 90 minutes via iPRISM cassettes, Adv. Sci. 2303285 (2023) 1–13.
[22] C.M. Svensson, et al., Coding of experimental conditions in microfluidic droplet assays using colored beads and machine learning supported image analysis, Small 15 (2019) 1–14.
[23] A. Ruszczak, S. Bartkova, M. Zapotoczna, O. Scheler, P. Garstecki, Droplet-based methods for tackling antimicrobial resistance, Curr. Opin. Biotechnol. 76 (2022) 102755.
[24] C.M. Ardila, G.A. Jiménez-Arbeláez, A.M. Vivares-Builes, The potential clinical applications of a microfluidic lab-on-a-chip for the identification and antibiotic susceptibility testing of enterococcus faecalis-associated endodontic infections: a systematic review, Dent. J. 12 (2023) 5.
[25] N. Qin, P. Zhao, E.A. Ho, G. Xin, C.L. Ren, Microfluidic technology for antibacterial resistance study and antibiotic susceptibility testing: review and perspective, ACS Sens. 6 (2021) 3–21.
[26] J. Campbell, et al., Microfluidic advances in phenotypic antibiotic susceptibility testing, Biomed. Micro 18 (2016) 103.
[27] P. Zhu, L. Wang, Passive and active droplet generation with microfluidics: a review, Lab Chip 17 (2017) 34–75.
[28] B. Li, et al., Droplets microfluidics platform-A tool for single cell research, Front. Bioeng. Biotechnol. 11 (2023) 1121870.
[29] F. Lyu, et al., Phenotyping antibiotic resistance with single-cell resolution for the detection of heteroresistance, Sens. Actuators B Chem. 270 (2018) 396–404.
[30] H. Wang, et al., Innovative optofluidics and microscopy-based rapid analysis of pathogens, Biomed. Opt. Express 11 (2020) 5060.
[31] Y. Lu, et al., Single cell antimicrobial susceptibility testing using confined microchannels and electrokinetic loading, Anal. Chem. 85 (2013) 3971–3976.
[32] J. Choi, et al., Rapid antibiotic susceptibility testing by tracking single cell growth in a microfluidic agarose channel system, Lab Chip 13 (2013) 280–287.
[33] Y. Jeong, et al., Color-Coded Droplets and Microscopic Image Analysis for Multiplexed Antibiotic Susceptibility Testing, Biosensors 11 (2021) 283.
[34] N. Pacocha, et al., High-Throughput Monitoring of Bacterial Cell Density in Nanoliter Droplets: Label-Free Detection of Unmodified Gram-Positive and Gram-Negative Bacteria, Anal. Chem. 93 (2021) 843–850.
[35] S. Hengoju, et al., Optofluidic detection setup for multi-parametric analysis of microbiological samples in droplets, Biomicrofluidics 14 (2020) 024109.
[36] X. Liu, et al., High-throughput screening of antibiotic-resistant bacteria in picodroplets, Lab Chip 16 (2016) 1636–1643.
[37] J.C. Stover. Optical Scattering: Measurements and Analysis, Third Edition, SPIE, 2012, https://doi.org/10.1117/3.975276.
[38] S. Maure, G. Albrand, C. Amra, Low-level scattering and localized defects, Appl. Opt. 35 (1996) 5573–5582.

[39] S. Schröder, M. Trost, T. Herffurth, A. von Finck, A. Duparré, Light scattering of interference coatings from the IR to the EUV spectral regions, Adv. Opt. Technol. 3 (2014) 113–120.
[40] M. Trost, et al., In situ and ex situ characterization of optical surfaces by light scattering techniques, Opt. Eng. 53 (2014) 92013.
[41] S. Schröder, A. Duparré, A. Tünnermann, Bewertung von Nanorauheiten durch Streulichtmessung (Nano-roughness Assessment by Light Scattering Measurement), Tm. - Tech. Mess. 73 (2006) 35–42.
[42] J.Q. Yu, et al., Droplet optofluidic imaging for λ-bacteriophage detection via co-culture with host cell Escherichia coli, Lab Chip 14 (2014) 3519–3524.
[43] A.S. Munser, et al., Analysis of very low bacterial counts in small sample volumes using angle-resolved light scattering, Appl. Opt. 62 (2023) 411–418.
[44] H.C. van de Hulst, Light Scattering by Small Particles, Dover Publications, 1981.
[45] C.F. Bohren, D.R. Huffman, Absorption and scattering of light by small particles, Wiley, 1983.
[46] A. Gupta, et al., Deep learning in image cytometry: a review, Cytom. Part A 95 (2019) 366–380.
[47] K. Paek, et al., A high-throughput biomimetic bone-on-a-chip platform with artificial intelligence-assisted image analysis for osteoporosis drug testing, Bioeng. Transl. Med. 8 (2022) e10313.
[48] Z. Li, F. Liu, W. Yang, S. Peng, J. Zhou, A survey of convolutional neural networks: analysis, applications, and prospects, IEEE Trans. Neural Netw. Learn. Syst. 33 (2022) 6999–7019.
[49] J.-P. Praetorius, K. Walluks, C.-M. Svensson, D. Arnold, M.T. Figge, IMFSegNet: Cost-effective and objective quantification of intramuscular fat in histological sections by deep learning, Comput. Struct. Biotechnol. J. 21 (2023) 3696–3704.
[50] A. Sarkar, J.-P. Praetorius, M.T. Figge, Deep learning-based characterization of neutrophil activation phenotypes in ex vivo human Candida blood infections, Comput. Struct. Biotechnol. J. 23 (2024) 1260–1273.
[51] J.P. Horwath, D.N. Zakharov, R. Mégret, E.A. Stach, Understanding important features of deep learning models for segmentation of high-resolution transmission electron microscopy images, npj Comput. Mater. 6 (2020) 108.
[52] H. Zhang, W.Y. Kendall, E.T. Jelly, A. Wax, Deep learning classification of cervical dysplasia using depth-resolved angular light scattering profiles, Biomed. Opt. Express 12 (2021) 4997–5007.
[53] A.S. Anker, K.T. Butler, R. Selvan, K.M.Ø. Jensen, Machine learning for analysis of experimental scattering and spectroscopy data in materials chemistry, Chem. Sci. 14 (2023) 14003–14019.
[54] T. Saba, Computer vision for microscopic skin cancer diagnosis using handcrafted and non-handcrafted features, Microsc. Res. Tech. 84 (2021) 1272–1283.
[55] M. Tovar, et al., 3D-glass molds for facile production of complex droplet microfluidic chips, Biomicrofluidics 12 (2018) 24115.
[56] S. Schröder, T. Herffurth, A. Duparré, G. Notni, Device and method for angularly resolved scattered light measurement, 00 2010, WO 127 (2010) 872.
[57] E. Zang, et al., Real-time image processing for label-free enrichment of Actinobacteria cultivated in picolitre droplets, Lab Chip 13 (2013) 3707–3713.
[58] M. Tan, Q. Le, EfficientNetV2: smaller models and faster training, Int. Conf. Mach. Learn. PMLR 139 (2021) 10096–10106.
[59] T. Hastie, J. Friedman, R. Tibshirani, The Elements of Statistical Learning: Data Mining, Inference, and Prediction, Springer, 2001, https://doi.org/10.1007/978-0-387-21606-5.
[60] M.Z. David, R.S. Daum, Community-associated methicillin-resistant Staphylococcus aureus: epidemiology and clinical consequences of an emerging epidemic, Clin. Microbiol. Rev. 23 (2010) 616–687.
[61] S.Y.C. Tong, J.S. Davis, E. Eichenberger, T.L. Holland, V.G.J. Fowler, Staphylococcus aureus infections: epidemiology, pathophysiology, clinical manifestations, and management, Clin. Microbiol. Rev. 28 (2015) 603–661.
[62] K. Hiramatsu, et al., Multi-drug-resistant Staphylococcus aureus and future chemotherapy, J. Infect. Chemother. 20 (2014) 593–601.
[63] The American Society of Health-System Pharmacists. Tetracycline. date accessed: *20.08.2024* ⟨https://medlineplus.gov/druginfo/meds/a682098.html⟩ (2017).
[64] Robert Koch Institute. RKI-Ratgeber Pest. date accessed: 20.08.2024 ⟨https://www.rki.de/DE/Content/Infekt/EpidBull/Merkblaetter/Ratgeber_Pest.html#doc10166986bodyText12⟩ (2017).
[65] Robert Koch Institute. RKI-Ratgeber Tularämie. date accessed: 20.08.2024 ⟨https://www.rki.de/DE/Content/Infekt/EpidBull/Merkblaetter/Ratgeber_Tularaemie.html#doc2398238bodyText12⟩ (2016).
[66] M. Carrel, et al., Antimicrobial resistance patterns of outpatient staphylococcus aureus isolates, e2417199–e2417199, JAMA Netw. Open 7 (2024). e2417199–e2417199.
[67] S. Ceballos, C. Aspiroz, L. Ruiz-Ripa, M. Zarazaga, C. Torres, Antimicrobial resistance phenotypes and genotypes of methicillin-resistant Staphylococcus aureus CC398 isolates from Spanish hospitals, Int. J. Antimicrob. Agents 55 (2020) 105907.
[68] A.M. Kaushik, et al., Accelerating bacterial growth detection and antimicrobial susceptibility assessment in integrated picoliter droplet platform, Biosens. Bioelectron. 97 (2017) 260–266.
[69] A.M. Kaushik, et al., Droplet-based single-cell measurements of 16S rRNA enable integrated bacteria identification and pheno-molecular antimicrobial susceptibility testing from clinical samples in 30 min, Adv. Sci. 8 (2021) 2003419.
[70] S. Rösner, et al., Evaluation of a novel immunochromatographic lateral flow assay for rapid detection of OXA-48, NDM, KPC and VIM carbapenemases in multidrug-resistant Enterobacteriaceae, J. Med. Microbiol 68 (2019) 379–381.
[71] A.R. Tuttle, N.D. Trahan, M.S. Son, Growth and maintenance of escherichia coli laboratory strains, Curr. Protoc. 1 (2021) e20.
[72] D.M. Missiakas, O. Schneewind, Growth and Laboratory Maintenance of Staphylococcus aureus, Curr. Protoc. Microbiol. 28 (Unit 9C) (2013) 1.
[73] M.I. Lanzl, M.H. Zwietering, W.C. Hazeleger, T. Abee, H.M.W. den Besten, Variability in lag-duration of Campylobacter spp. during enrichment after cold and oxidative stress and its impact on growth kinetics and reliable detection, Food Res. Int. 134 (2020) 109253.
[74] W. Postek, P. Gargulinski, O. Scheler, T.S. Kaminski, P. Garstecki, Microfluidic screening of antibiotic susceptibility at a single-cell level shows the inoculum effect of cefotaxime on E. coli, Lab Chip 18 (2018) 3668–3677.
[75] P. Zhang, et al., A cascaded droplet microfluidic platform enables high-throughput single cell antibiotic susceptibility testing at scale, Small Methods 6 (2022) 2101254.
[76] J.Q. Boedicker, L. Li, T.R. Kline, R.F. Ismagilov, Detecting bacteria and determining their susceptibility to antibiotics by stochastic confinement in nanoliter droplets using plug-based microfluidics, Lab Chip 8 (2008) 1265–1272.
[77] L. Mahler, et al., Highly parallelized droplet cultivation and prioritization of antibiotic producers from natural microbial communities, Elife 10 (2021) e64774.

Martina Graf: 2015–2020 BSc and MSc studies in Biotechnology at Technical University of Braunschweig, Germany. Since 2021 PhD studies in the microfluidics group at the Bio Pilot Plant of Leibniz-HKI and at the Friedrich Schiller University, Jena, Germany.

Arjun Sarkar: 2018–2021 MSc in Biomedical Engineering at FH Aachen University of Applied Science, Aachen, Germany. Since 2021 PhD student at Image Analysis group of Applied Systems Biology, Leibniz Institute for Natural Product Research and Infection Biology - Hans Knöll Institute and Friedrich Schiller University, Jena, Germany.

Carl-Magnus Svensson: 2009 PhD in Applied Mathematics at University of Nottingham, Nottingham, UK. 2009–2011 Research Fellow, School of Psychology, University of Nottingham, Nottingham. 2011–2012 Researcher, Frankfurt Institute for Advanced Studies (FIAS), Frankfurt, Germany. Since 2012 Researcher at the research group Applied Systems Biology at Leibniz Institute for Natural Product Research and Infection Biology - Hans Knöll Institute, Jena, Germany

Anne-Sophie Munser: 2016 M.Eng in Laser- and Optotechnologies from the University of Applied Sciences Jena. Since 2017, scientist at Fraunhofer IOF for Applied Optics and Precision Engineering, Jena. 2024 PhD in Optics from the Friedrich-Schiller University, Jena.

Sven Schröder: 2008 PhD in Physics from the Friedrich-Schiller University, Jena. Since 2016, head of the Surface and Thin Film Characterization Group and since 2019, head of department Functional Surfaces and Coatings at Fraunhofer IOF for Applied Optics and Precision Engineering in Jena.

Sundar Hengoju: 2007–2011 BTech in Biotechnology, Kathmandu University, Nepal; 2013–2015 Studies in Biochemistry (MSc) at Chungbuk National University, South Korea. 2016–2020 PhD studies at Bio Pilot Plant of the Leibniz-HKI and Friedrich Schiller University of Jena. Since 2020 Postdoc at Leibniz-HKI, Jena for droplet-based microfluidics.

Miriam A. Rosenbaum: 1999–2004 Diploma Studies in Biochemistry at the University of Greifswald, 2006 PhD in Environmental Chemistry at the same place. 2007–2011 Postdoc Washington University and Cornell University, USA. 2011–2017 Assistant Professor in Applied Microbiology at the RWTH Aachen. Since 2017 Professorship for Synthetic Biotechnology at Friedrich Schiller University of Jena and Department Chair of the Bio Pilot Plant at Leibniz-HKI, Jena, Germany.

Marc Thilo Figge: 2000 PhD in Theoretical Physics at the Rijksuniversiteit Groningen, The Netherlands. Since 2011 professor at the Friedrich Schiller University, Jena, Germany and head of research group Applied Systems Biology at Leibniz Institute for Natural Product Research and Infection Biology - Hans Knöll Institute, Jena, Germany.